PNAS RESEARCH ARTICLE | APPLIED PHYSICAL SCIENCES

Melting of nonreciprocal solids: How dislocations propel and fission in flowing crystals

Stéphane Guillet[a,1], Alexis Poncet[a,1,2], Marine Le Blay[b,1], William T. M. Irvine[c,d], Vincenzo Vitelli[c,d], and Denis Bartolo[a,2]

Affiliations are included on p. 9.

Edited by Sriram Ramaswamy, Indian Institute of Science, Bangalore, India; received July 9, 2024; accepted March 8, 2025 by Editorial Board Member Paul Chaikin

When soft matter is driven out of equilibrium its constituents interact via effective interactions that escape Newton's action–reaction principle. Prominent examples include the hydrodynamic interactions between colloidal particles driven in viscous fluids, phoretic interactions between chemically active colloids, and quorum-sensing interactions in bacterial colonies. Despite a recent surge of interest in nonreciprocal physics, a fundamental question remains: do nonreciprocal interactions alter or strengthen the ordered phases of matter driven out of equilibrium? Here, through a combination of experiments and simulations, we show how nonreciprocal forces propel and fission dislocations formed in hydrodynamically driven Wigner crystals. We explain how dislocation motility results in the continuous reshaping of grain-boundary networks, and how their fission reaction melts driven crystals from their interfaces. Beyond the specifics of hydrodynamics, we argue theoretically that topological defects and nonreciprocal interactions should invariably conspire to deform and ultimately destroy crystals.

nonreciprocal interactions | colloidal crystal | topological defects | hydrodynamic melting

Significance

When matter is driven out of equilibrium, its elementary units can experience effective forces that evade an action–reaction principle. Prominent examples include hydrodynamic interactions mediated by fluid flows, chemotactic interactions between chemically active units, and cognitive interactions among living organisms. Understanding how the states of nonequilibrium matter are altered by the competition between nonreciprocal and conservative forces is a fundamental challenge. To make progress, we drive crystals with fluid flows and demonstrate that hydrodynamic interactions can continuously reshape their grain boundary networks and even disrupt crystalline order. Beyond the specifics of hydrodynamic interactions, we expose a theory that elucidates how nonreciprocal forces propel and fission dislocations in nonequilibrium crystals.

In our daily experiences, we accurately perceive Newton's laws of mechanics: we do not feel any force as we travel at constant speed in a train, we feel a force when it accelerates, and we feel the backreaction of our seat on our back as we compress it with our body weight. However, our intuition is significantly challenged when trying to understand the behavior of systems composed of many interacting bodies, for which we only have access to a small subset of their degrees of freedom. Consider the simple example of two rigid particles falling in a viscous fluid under the sole action of gravity. It is surprising to observe that their speed and trajectory depend on their relative positions (1, 2). Two beads making a finite angle with the vertical axis do not even fall straight. The reason for this counterintuitive behavior is that our observations ignore the many degrees of freedom of the surrounding fluid. As a bead falls, it couples to the fluid flow, which in turn induces a drag force on the second particle. This dynamical coupling is commonly referred to as a hydrodynamic interaction (1, 3). However, unlike all conservative forces that derive from an energy potential, hydrodynamic interactions do not obey Newton's action–reaction principle. The drag forces induced by the two particles on one another are not opposite: hydrodynamic interactions are nonreciprocal.

Beyond hydrodynamics, nonreciprocal interactions rule the dynamics of systems as diverse as chemically active colloids (4, 5), coupled robots (6, 7), and interacting living creatures, from bacteria (8), to birds (9) and human beings (10).

The impact of nonreciprocal forces on many-body physics offers some formidable problems in fluid mechanics, soft condensed matter, and statistical mechanics. Even in the paradigmatic situation where a collection of underdamped particles are uniformly driven in a viscous fluid, their trajectories do not form mere straight lines, they are chaotic and strongly correlated in space and time (11–13). After decades of intense studies, the anomalous statistics of the velocity fluctuations, and the structural arrangements of hydrodynamically coupled bodies are yet to be elucidated and cannot be captured by an effective (Maxwell–)Boltzmann statistics. Even when they are arranged on a perfect periodic lattice, the dynamics of particles driven in viscous fluids remains highly counterintuitive. In the absence of any stabilizing elastic forces, theory predicts that fluctuations in the particle positions can cause the propagation of singular sound waves despite the irrelevance of inertia, or be amplified to destroy their spatial ordering (14–18).

In this article, our objective is to answer a fundamental question which remains unsolved despite a growing interest in non reciprocal matter; see, e.g., refs. 19–31: how

Author contributions: D.B. designed research; S.G., A.P., and M.L.B. performed research; S.G., A.P., M.L.B., and D.B. analyzed data; S.G., A.P., M.L.B., W.T.M.I., V.V., and D.B discussed the results; and S.G., A.P., and D.B. wrote the paper.

The authors declare no competing interest.

This article is a PNAS Direct Submission. S.R. is a guest editor invited by the Editorial Board.

[1]S.G., A.P., and M.L.B. contributed equally to this work.

[2]To whom correspondence may be addressed. Email: alexis.poncet@ens-lyon.fr or denis.bartolo@ens-lyon.fr.

This article contains supporting information online at https://www.pnas.org/lookup/suppl/doi:10.1073/pnas.2412993122/-/DCSupplemental.

Published April 11, 2025.

do fluctuations powered by nonreciprocal forces alter the ordered phases of soft matter? To make progress, we consider a basic situation where crystalline order is stabilized by conservative forces and undermined by hydrodynamic interactions. We establish two universal results through the combination of experiments, numerical simulations, and mathematical modeling: i) Nonreciprocal interactions sustain the continuous reshaping of the grain boundaries that separate crystals of incompatible orientations. ii) When nonreciprocal forces overcome elastic interactions, they split dislocations into pairs and cause their exponential proliferation. This nonequilibrium 2D melting process escapes the standard KTHNY (32–34) and hydrodynamic clumping scenarios (12, 14, 18).

We organize the presentation of our results as follows. We start with an introduction of our experiments based on driven crystalline emulsions, and our numerical model, providing a bird's-eye view of our main findings. Next, we thoroughly characterize the dislocation dynamics and melting of driven polycrystals in response to nonreciprocal hydrodynamic interactions. Finally, we conclude with a general discussion. Beyond the specifics of our experiments, we explain how the interplay between dislocation dynamics and nonreciprocal forces governs the behavior of a broad class of nonequilibrium crystals, where conservative forces compete with nonreciprocal interactions arising from hydrodynamic, mechanical, chemical, or cognitive couplings.

Driving Wigner Crystals Out of Equilibrium with Fluid Flows: Experiments, Simulations, and Main Findings

Experiments. We study the dynamics and structure of hydrodynamically driven crystals through the experiment shown in Fig. 1 and detailed in *SI Appendix*. In short, we assemble 2D Wigner crystals, by applying a uniform magnetic field to a paramagnetic emulsion confined in a microfluidic Hele-Shaw cell sketched in Fig. 1*B*. The resulting magnetic forces between the droplets (radius 33 μm) are isotropic, repulsive, and decay as $1/r^4$, Fig. 1*A*. They classically lead to the formation of pristine crystallites of incompatible orientations separated by grain boundaries, Fig. 1*A*. Variations of this standard setup have been instrumental to shed light on the statistics and kinetics of thermal melting in two dimensions (35–38). Here, we drive the system out of equilibrium with a pressure gradient transverse to the magnetic field. In the absence of droplets, the pressure drop results in a uniform flow of the continuous phase along the x direction, Fig. 1*B*. However, the droplets do not behave as passive tracers. Due to viscous friction on the confining walls, they are advected at a speed that is about two times smaller than the average flow (39). This velocity mismatch is key to inducing nonreciprocal interactions. Each droplet deforms the otherwise uniform flow and yield dipolar recirculations that decay algebraically in space as $1/r^2$, see, e.g., ref. 15. The droplets are then advected both by the mean flow and the dipolar disturbances induced by the surrounding particles. To demonstrate the relevance of these hydrodynamic interactions, we measure the time-averaged displacement of the droplets in a reference frame moving with a tagged particle. Fig. 1*C* shows that, when $B = 0\,\mathrm{mT}$, the particle trajectories are clearly perturbed by dipolar recirculations (see also *SI Appendix*). Crucially, as illustrated in Fig. 1*D*, when two particles are advected by these hydrodynamic perturbations, the resulting drag forces have equal magnitudes but not opposite directions. Unlike magnetic forces, hydrodynamic forces do not obey Newton's action–reaction principle. They are nonreciprocal.

We study the competition between the reciprocal (magnetic) and nonreciprocal (hydrodynamic) interactions by tuning their relative magnitude. We keep the mean-flow speed constant (corresponding to a mean droplet speed of $U = 150 \pm 1\,\mu\mathrm{m/s}$) and vary the strength of the $\mathbf{B}$ field between $B = 0\,\mathrm{mT}$ to $B = 10\,\mathrm{mT}$ using a 50 cm cylindrical coil. All the results presented in the main text correspond to experiments where the packing fraction is set to $\Phi = 0.37$ in the main channel. We keep the packing fraction constant throughout the experiments, by continuously injecting droplets in the main channel as we drive the emulsions. In *SI Appendix*, we provide a comprehensive description of our experimental setup and report a second series of experiments where $\Phi = 0.61$. None of our observations and conclusions crucially depend on these values.

Main Findings: Living Grain Boundaries and Hydrodynamic Melting. Before delving into a more thorough discussion, we first offer a bird's-eye view of our main findings. We invite the reader to watch Movies S1 and S2 first to have a clear visual impression of the polycrystals' structure and dynamics. We summarize them in the series of snapshots shown in Fig. 2. For the strongest value of the magnetic field ($B = 10\,\mathrm{mT}$), the fluid flow leaves the crystal order unchanged, Fig. 2*A*. However, despite the uniform drive, the polycrystals are not merely advected at constant speed. They feature a lively inner dynamics that continuously remold the grain-boundary network, the orientation of the crystal patches, and the distribution of their point defects. In the next sections, we explain why and how the action of hydrodynamic interactions on dislocations powers and sustains their gliding dynamics.

Movie S2 and Fig. 2*B* illustrate our second main finding. They show four steady states corresponding to decreasing values of the magnetic field. Although temperature is irrelevant in our system of non-Brownian droplets, we observe that crystalline order is progressively lost as B decreases. The grain size shrinks, while the level of orientational order and the lattice spacing within the crystallites remain unchanged, until they vanish. In the next sections, we show that nonreciprocal forces are responsible for a two-way coupling between the crystal structure and dynamics, and explain how they lead to the proliferation of dislocations and grain boundaries.

Numerical Simulations. Before quantifying and explaining our experimental findings, we first show that our observations do not depend on the specifics of our experiments, and are generic to the competition between stabilizing repulsive interactions and dipolar nonreciprocal forces. To do so, we introduce a minimal model that correctly captures all our experimental findings. We consider the overdamped dynamics of a collection of point particles labeled by their 2D position $\boldsymbol{R}_i(t)$ in a periodic domain. In the frame moving at the average particle speed, their equations of motion take the simple form:

$$\zeta \partial_t \mathbf{R}_i(t) = \sum_j \boldsymbol{F}_{\mathrm{core}}(\mathbf{R}_{ij}) + \boldsymbol{F}_{\mathrm{mag}}(\mathbf{R}_{ij}) + \boldsymbol{F}_{\mathrm{hydro}}(\mathbf{R}_{ij}), \quad [1]$$

where ζ is a friction coefficient and $\mathbf{R}_{ij} = \mathbf{R}_i - \mathbf{R}_j$. In all that follows, units are chosen so that $\zeta = 1$. The contact interactions between the droplets are accounted for by a short-range repulsive force $\boldsymbol{F}_{core}$ (WCA potential) that defines the particles' radius a. We model the magnetic interactions by

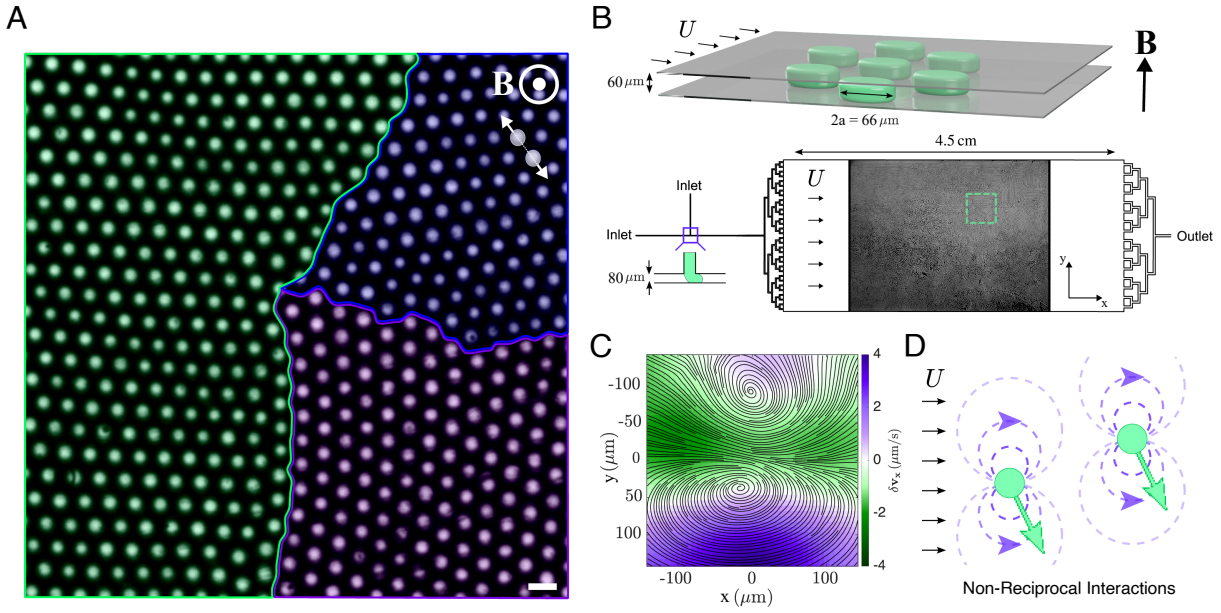

Fig. 1. Experimental system: hydrodynamically driven Wigner crystals. (*A*) Experimental image of a two-dimensional collection of hexadecane droplets dispersed in an aqueous ferrofluid. When applying a magnetic field, the droplets repel one another (white arrows), and self-organize into Wigner crystals separated by grain boundaries. The color shade indicates the orientation of the principal axis of the crystallites. The white arrows indicate that the magnetic repulsion between the dipoles obey Newton's action–reaction principle. (Scale bar, 150 μm.) (*B*) Schematics of our microfluidic device. We continuously produce a monodisperse emulsion at a T-junction and fill a 4.5 cm long Hele-Shaw cell. The oil droplets are confined by the two vertical walls and have a pancake shape. The device is placed in an electric coil; the resulting magnetic field **B** points in the direction transverse to the confining walls and induces repulsive interactions between the drops. The resulting polycrystal is advected at constant flow rate by a homogeneous plug flow **U** that points in the *x* direction (horizontal arrows). (*C*) Streamlines of the velocity field constructed from the droplets' motion. To quantify the hydrodynamic interactions, we track a droplet and use it to define a reference frame. We measure the velocity of all the surrounding droplets in this moving frame. We then construct the corresponding velocity field and time average it. We also average the droplet-velocity field over hundreds of different reference droplets. We can clearly see that the dominant contribution to the hydrodynamic interactions has a dipolar symmetry. The color indicates the magnitudes of the longitudinal velocity in the moving frame. (*D*) Sketch of the far-field hydrodynamic force field around two droplets. The hydrodynamic interactions do not obey Newton's third law: they are nonreciprocal.

the repulsion between point dipoles oriented in the direction transverse to the *xy*-plane: $\boldsymbol{F}_{\mathrm{mag}}(\boldsymbol{r}) = -\mathcal{B}\nabla\|\boldsymbol{r}\|^{-3}$, where $\mathcal{B}$ quantifies the repulsion strength. Finally, guided by previous models of interacting microfluidic droplets (15, 39), we ignore all near-field hydrodynamic contributions and describe the hydrodynamic interactions by their far-field component (Fig. 1*D*): $\boldsymbol{F}_{\mathrm{hydro}}(\boldsymbol{r}) = \nabla\frac{x}{2\pi r^2}$ that has an in-plane dipolar symmetry. Although $\boldsymbol{F}_{\mathrm{hydro}}(\boldsymbol{r})$ can be written as a gradient of a scalar quantity, we stress that it does not obey Newton's third law as $\boldsymbol{F}_{\mathrm{hydro}}(\boldsymbol{R}_{ij}) = \boldsymbol{F}_{\mathrm{hydro}}(\boldsymbol{R}_{ji})$. $\boldsymbol{F}_{\mathrm{hydro}}$ is nonreciprocal. We solve Eq. **1** numerically using a modified Ewald algorithm detailed in *SI Appendix*. In all our simulations, we set the value of a so that the equivalent packing fraction matches our experimental value. We are thus left with a single parameter $\mathcal{B}$ that plays the same role as the magnitude of the B field in our experiments. It quantifies the relative magnitude of the reciprocal and nonreciprocal interactions.

The repulsive interactions organize the particles into a Wigner polycrystal. However, in agreement with our experiments, even when the repulsive forces overcome the nonreciprocal interactions, the polycrystals continuously reorganize the shape of their grain boundaries, and their topological defect distributions, Fig. 2*A*. Further decreasing $\mathcal{B}$, the grains' size shrinks until the point where crystalline order is fully destroyed at all scales, Fig. 2*C*.

The consistency between our experimental and numerical observations unambiguously confirms that the inner dynamics and melting of our driven crystals originate from the competition between potential and nonreciprocal interactions.

Results

Nonreciprocal Interactions Propel and Remold Grain Boundaries. Our first goal is to quantify and explain the self-sustained dynamics of the grain boundary network in the ordered/polycrystal phase (Fig. 2*A* and Movie S1). By definition, the grain boundaries separate regions of incompatible crystal orientations. We can therefore quantify their dynamics by measuring the fluctuation spectrum of the orientational (hexatic) order parameter ψ_6; see also *SI Appendix*. Fig. 3*A* shows the spectrum corresponding to wave vectors $\mathbf{q} = q\hat{\mathbf{x}}$ pointing along the flow direction. The spectrum is peaked on a curve which shows that the fluctuations of the hexatic order parameter are not merely overdamped but propagate. The ψ_6 waves, however, do not merely reflect the homogeneous advection of the polycrystal. We plot their dispersion relation in Fig. 3*B* and find that the speed of the orientational-wave c_6 (the slope at the origin of the dispersion relation) is always negative, Fig. 3*C*. In other words, the fluctuations of the crystals' orientation, and therefore of the grain boundaries, propagate against the fluid flow. This finding is further confirmed by tracking the trajectories of the disclinations defined as the Voronoï cells having a number of edges smaller or larger than six. The distributions of the disclination velocity are broad (*SI Appendix*). But, in the longitudinal direction, the speed peaks at a value which is again systematically smaller than the average drop speed U, Fig. 3*D*. The elementary topological defects propagate upstream, however they do not merely translate but also continuously reorganize the structure of the grains. To elucidate this complex dynamics, we now take advantage of our numerical simulations. Unlike in experiments, we can

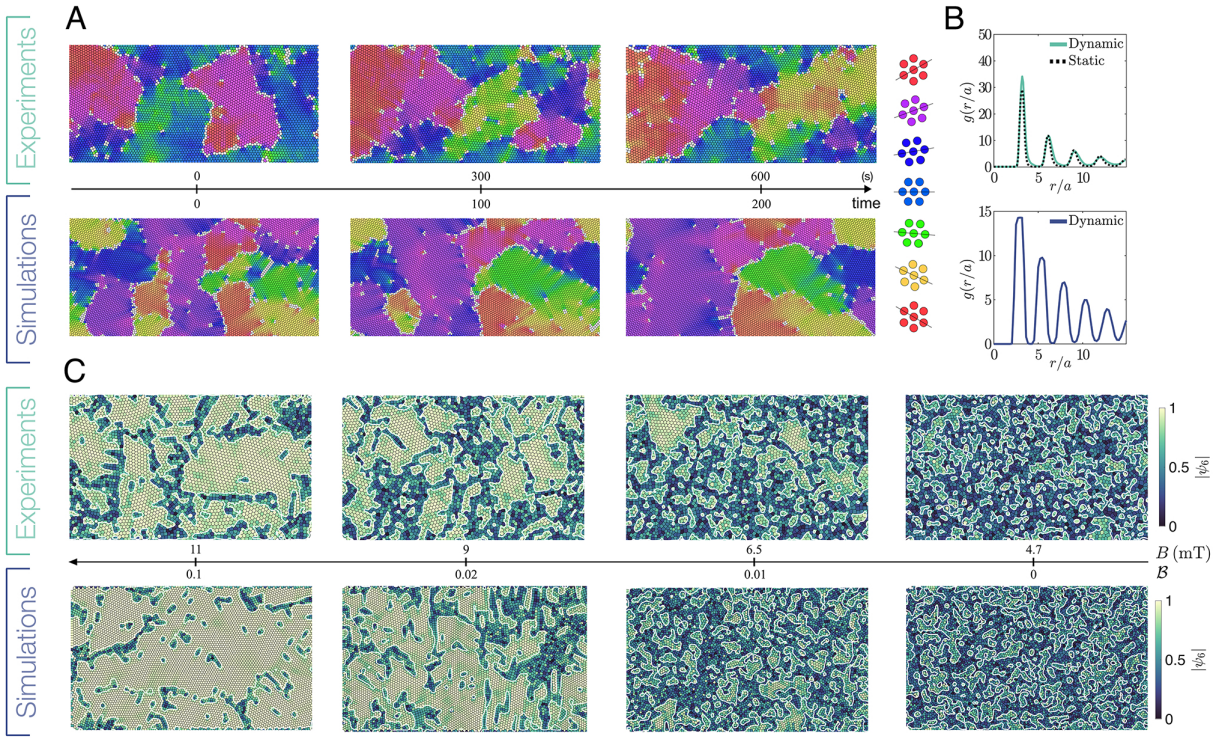

Fig. 2. Polycrystals dynamic: experiments vs. numerics. (*A*) Four subsequent snapshots of the crystal-orientation field defined as the phase θ_6 of the hexatic order parameter ψ_6 (40). Top row: experiments. Bottom row: numerical simulations. Both our experiments ($B = 9.7$ mT) and simulations ($\mathcal{B} = 0.2$) reveal that the driven polycrystals continuously reshape the geometry of their grain boundaries. The θ_6 field is defined at the scale of the Voronoï cells computed from the center of mass of the drops. The grain boundaries are defined by the cells where $|\psi_6| < 0.6$. (*B*) Variations of the pair-correlation function $g(\mathbf{r})$ along the local principal axis of the crystals. The hydrodynamic flows hardly alter the inner structure of the crystallites. (*C*) Variations of the local magnitude of the ψ_6 order parameter in our experiments and simulations. Upon decreasing the magnitude of the repulsive magnetic interactions, the system transitions from an ordered hexagonal state to a disordered liquid state. The white lines indicate the position of the grain boundaries.

prepare two pristine Wigner crystals separated by two straight grain boundaries orthogonal to the flow. We can then let them evolve under the action of the nonreciprocal forces. In Fig. 3 *E* and *F* and Movie S3, we observe that the grain boundaries and the associated ψ_6 fluctuations propel steadily in the upstream direction. We then repeat this measurement for grain boundaries forming a finite angle β with the flow as illustrated in Fig. 3*G*. We find that their shape remains unchanged but that their speed varies with β; see Fig. 3*H*. Consequently, curved grain boundaries must deform as confirmed by the simulations of a circular grain showed in Fig. 3*I* and Movie S4. Our recent theory exposed in ref. 27, provides an explanation for the motility of the grain boundaries. We recall and generalize it in *SI Appendix*. In short, when a dislocation of Burgers vector $\mathbf{b}$ forms in a crystal, it causes elastic deformations at all scales. The resulting strain induces nonreciprocal interactions between the particles that build an effective Peach–Köhler force $\mathbf{F}^{PK}$ acting on the dislocation (27, 41). $\mathbf{F}^{PK}$ decomposes into a glide $F^{PK}_{glide} = \mathbf{F}^{PK}\cdot\hat{\mathbf{b}}$ and a climb component $F^{PK}_{climb} = \mathbf{F}^{PK}\cdot\hat{\mathbf{b}}^{\perp}$. When the nonreciprocal forces originate from dipolar hydrodynamic interactions ($\boldsymbol{F}_{hydro}$), the total Peach–Köhler force points along the flow direction and the glide component reduces to

$$\mathbf{F}^{PK}_{glide} \propto -(\mathbf{b}\cdot\hat{\mathbf{x}})\boldsymbol{b}. \qquad [2]$$

This relation captures all the ingredients needed to explain our first set of experimental and numerical observations: i) $\mathbf{F}^{PK}_{glide}$ points in the direction opposite to the driving flow. It therefore powers the upstream motion of any dislocation whose burgers vector does not make a $\pi/2$ angle with the horizontal direction. ii) The magnitude of the Peach–Köhler force depends on the orientation of the dislocations. In agreement with our experimental and numerical results reported in Fig. 3, ignoring the effect of elastic interactions between the dislocations, Eq. **2** indicates that straight grain boundaries should propagate steadily against the macroscopic drive, whereas curved grains should deform under the action of the hydrodynamic interactions.

Nature of the Hydrodynamic Melting of Wigner Polycrystals. We have demonstrated that nonreciprocal interactions sustain the continuous remolding of domain walls in hydrodynamically driven crystals. We now ask how nonreciprocal interactions disrupt crystalline order as elastic interactions weaken (Fig. 2*C*). To answer this question, we first characterize the evolution of translational and orientational order parameters in steady state as we gradually decrease the magnitude of the magnetic forces. We then explain our findings, and explain how the hydrodynamic interactions promote dislocation splitting and govern the melting process.

To characterize the structural evolution of our emulsions, we plot the pair correlation functions of the droplets for different values of the *B* field (experiments and simulations), Fig. 4*A*. As the elastic forces weaken, the amplitude of the crystal peaks decreases continuously, Fig. 4*B*. However, at high *B*, the locations of the peaks do not vary, and no new structural feature emerges: the local symmetry and period of the crystals remain the same, Fig. 4*C*. This observation is at odds with the clumping-induced-melting scenario reported in various hydrodynamic crystals, from the early experiments of Crowley (14), to the numerical simulations

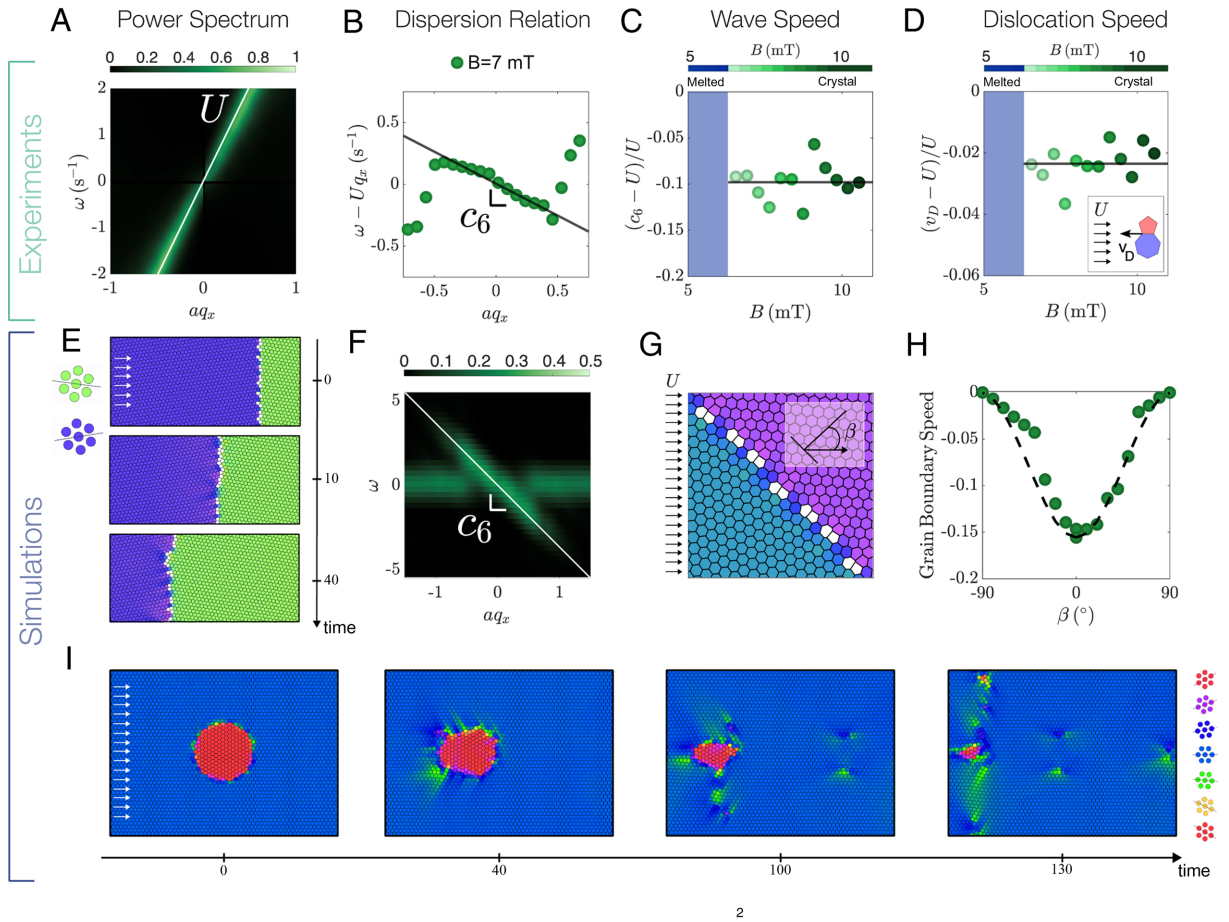

Fig. 3. Orientational waves and dislocation glide. (*A*) Power spectrum of the ψ_6 field $\langle|\psi_6(q_x,\omega)|^2\rangle$, where q_x represent the wave vectors in the flow direction and ω the time frequency. The power spectrum is peaked on a line in the (q_x,ω) plane. (*B*) This line is however not straight and defines the dispersion relation of the orientational waves. The wave speed corresponds to its slope at the origin and we measure it in the frame moving with the average droplet speed $U = 150 \pm 1$ μm/s. Experiments performed at $B = 7$ mT (*C*) c_6 is negative for all B values: in the comoving frame, orientation waves propagate upstream. (*D*) We define the speed of the disclinations v_D as the location of the peak of their velocity distribution along the x axis. v_D is systematically smaller than U in the polycrystal phase. (*E*) Simulation of the dynamics of a straight grain boundary ($\mathcal{B} = 0.2$). The interface between the two crystals is stable but propagates upstream. (*F*) ψ_6 power spectrum corresponding to the numerical simulations of *E*. Hexatic waves propagate upstream. (*G* and *H*) Speed of the straight grain boundary plotted against its orientation with the mean flow (Simulations). The dashed line corresponds to our theoretical prediction ($-\cos\beta$ function). (*I*) Simulation of a circular grain. The grain shape is not stable, it undergoes self-sustained deformations powered by the nonreciprocal forces ($\mathcal{B} = 0.1$).

of ref. 18 (see also refs. 12 and 42). Further decreasing B, the structure of the emulsion then changes sharply, Fig. 4*C*. When $B < B_g = 3.25\,mT$, no crystallite survives, the crystal peaks vanish, and we are left with a fully disordered liquid whose structure hardly depends on B, Fig. 4*A*.

The evolution of the orientational order parameter provides another insight into the melting process. In Fig. 4*D*, we plot the distributions of magnitude of the local ψ_6 field. When the elastic interactions are strong (high B), the distributions peak at a value close to one. The location of the ψ_6 peak hardly shifts toward smaller values until $B = B_6 = 6.4$ mT (experiments), Fig. 4*E*. It then discontinuously drops to reach a value close to the maximum of the ψ_6 distribution computed for a Poisson point process. These variations provide a clear definition of the crystalline clusters: they correspond to regions where the value of ψ_6 exceeds 0.6. In Fig. 4*F*, we plot the correlation length of the orientational order parameter ξ_6 against B. We find that, for strong magnetic repulsion, ξ_6 continuously decreases while the magnitude of the orientational order parameter remains nearly constant (Fig. 4 *B* and *F*). We therefore conclude that the loss of orientational order does not happen within the crystal patches, but reflects their shrinking as B decreases. As the hydrodynamic interactions prevail over the elastic forces, a sea of liquid phase grows around nearly pristine crystallites whose size shrinks in response to nonreciprocal interactions.

To further confirm the prominent role played by grain boundaries in our melting process, we take advantage of our numerical simulations. We start with two crystals separated by two straight interfaces, and quench the system right below the "melting point," $\mathcal{B} = 17 \times 10^{-3}$ in our simulations. Fig. 5*A* clearly reveals that topological defects hardly ever nucleate in the bulk but proliferate from the grain boundaries. Ultimately, in agreement with our experimental observations, the defect proliferation leads to a macroscopic reshaping of the polycrystal geometry and leads to the formation of small ordered clusters that coexist with macroscopic disordered regions.

To elucidate this melting process, we consider the even simpler case of an isolated dislocation; see Fig. 5*B*. When $\mathcal{B}$ is set right below the melting point $\mathcal{B}_6$, we find that at early times, the dislocation fissions to form a pair of gliding defects. We can understand this fission process as follows. The sum of the hydrodynamic interactions acting around a dislocation results in an effective Peach–Köhler force that includes a climb component:

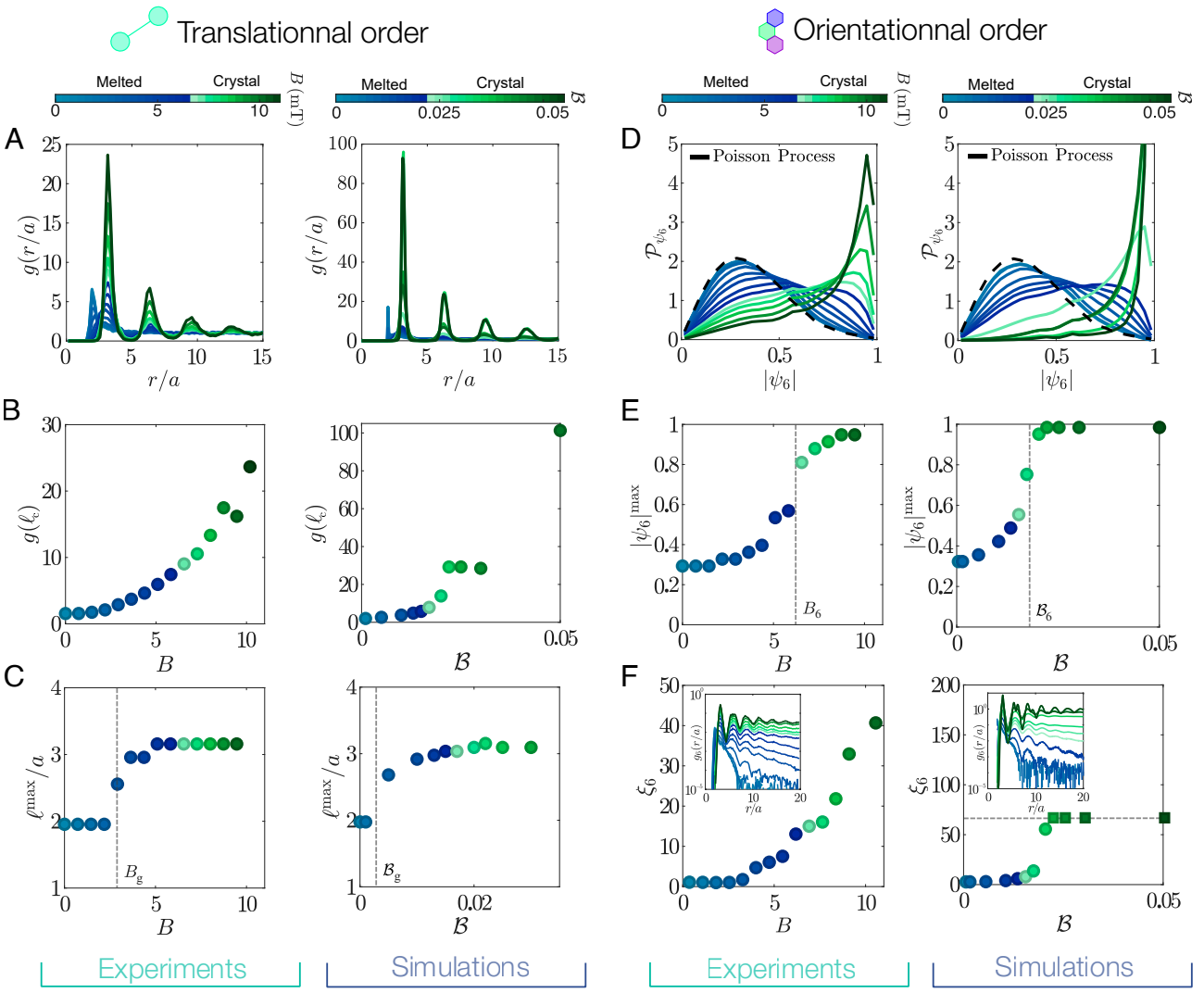

Fig. 4. Hydrodynamic melting. (*A*) Pair correlation functions $g(r/a)$ measured along the direction defined by the local value of θ_6. $g(r/a)$ is plotted for different values of the applied magnetic field. The structure evolves from a crystal to a liquid. Experiments and simulations. (*B*) Variations of the amplitude of the first crystal peak $g(\ell_c)$ with *B*. The position ℓ_c of the first crystal peak is defined in panel *A*. Experiments and simulations. (*C*) The position of the first peak of $g(r/a)$ ($\ell^{\max}$) does not vary with over a range of *B* values. The structure of the Wigner crystals does not change in the bulk as *B* decreases. Experiments and simulations. (*D*) Distribution of the magnitude of the local and instantaneous hexatic field $\psi_6(\mathbf{r}, t)$. The dashed line indicates the same distribution computed for a random set of points (2D Poissonian process). Experiments and simulations. (*E*) Evolution of the position of the maximum of the ψ_6 distribution with the magnitude of the repulsive interactions. Experiments and simulations. The position of the ψ_6 maximum clearly signals the melting point of the polycrystal structure. (*F*) The correlation lengths ξ_6 associated with the spatial correlations of ψ_6 (*Inset*) continuously decrease as the strength of the repulsive force decreases and the polycrystal melts. Experiments and simulations. In our simulations ξ_6 plateaus at high $\mathcal{B}$ values as it reaches the system size.

$$\mathbf{F}^{PK}_{climb} \propto -(\mathbf{b}^{\perp} \cdot \hat{\mathbf{x}})\boldsymbol{b}^{\perp}, \qquad [3]$$

where **b** is the Burgers vector. However, a dislocation cannot propel along the climb direction due to the extensive energy cost associated with their displacement. In agreement with the optical tweezer experiments reported in ref. 43, we find that above a critical local strain, an isolated dislocation reacts by fissioning into a defect pair, keeping the overall topological charge constant; see Fig. 5*B*. At later times, the propulsion of the dislocation pair, their interactions, and subsequent fission reactions result in a complex chain reaction that gradually destroys the crystal ordering.

We stress that the defect-splitting process rules the melting dynamics, as the bulk of our hydrodynamic crystal is stable. In a perfect periodic lattice the sum of all hydrodynamic interactions cancel out exactly, and governs a dynamic that is linearly stable to structural fluctuations; see ref. 16 and 18 and *SI Appendix*.

In sum, the melting process that we have uncovered is typical of driven nonequilibrium matter whose inner structure and dynamics cannot be disentangled. As dislocations form, the changes in the crystal structure induce hydrodynamic forces that alter the particle dynamics and fluid flows. The flows cause the fission of the dislocations. These structural changes then feedback again on the particle dynamics thereby leading to a cascade of fission and annihilation events that dynamically shape the structure of the polycrystals.

This melting process is markedly different from the entropic proliferation of topological defects in the bulk of thermal 2D crystals (40). It is however reminiscent of the nucleation of dynamical crystals in collections of dense self-propelled hard disks (44), and the suppression of order from living grain boundaries is strikingly similar to the melting of odd colloidal crystals reported in ref. 45. This resemblance is not anecdotal and hints toward seemingly similar mechanisms which we discuss in the next section.

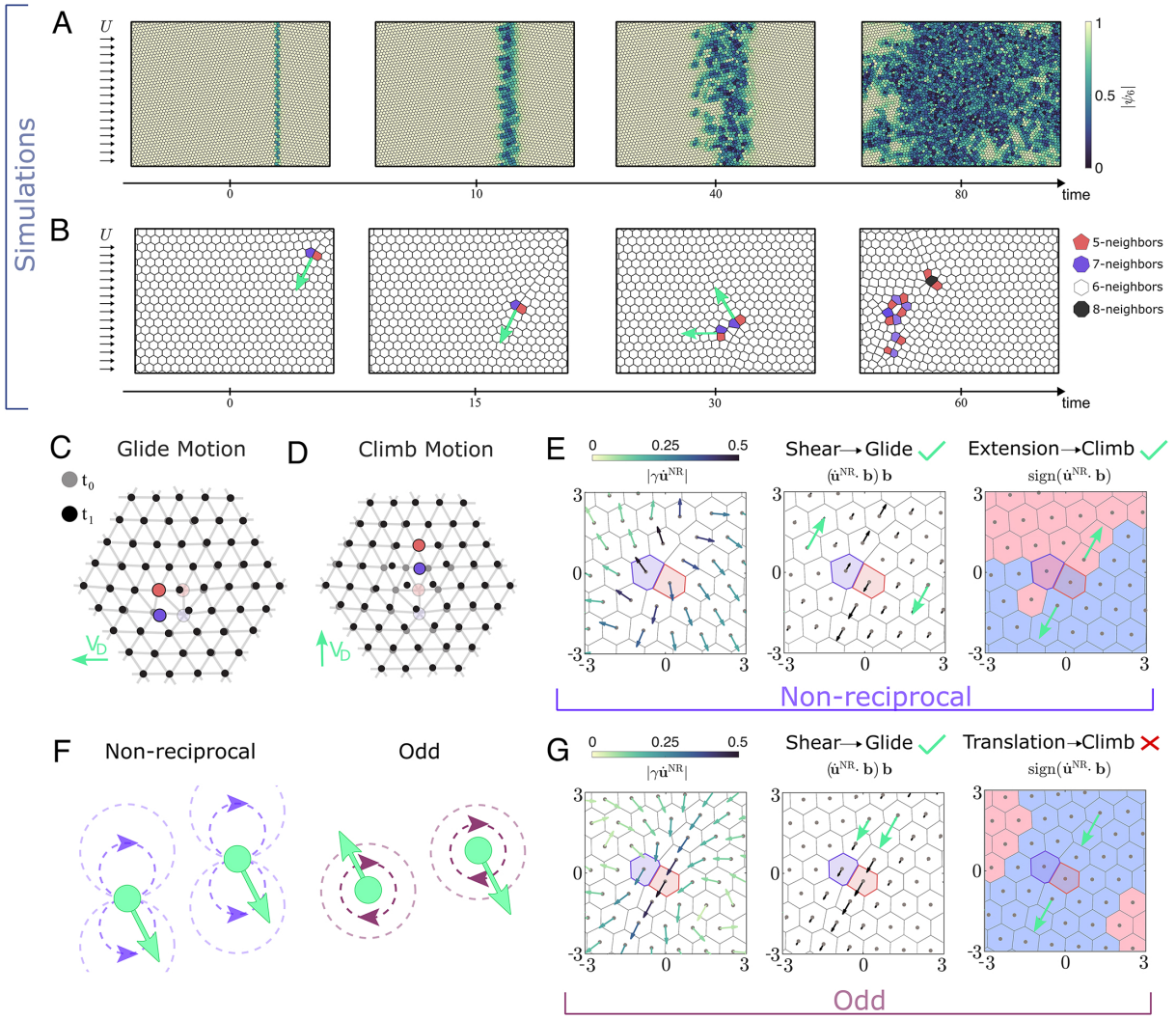

Fig. 5. Nonreciprocal forces split dislocations. (*A*) Structural evolution of two crystals separated by a straight grain boundary upon a rapid quench. We initialize the system by relaxing the elastic energy ($\mathcal{B} = 0$), we then turn on the nonreciprocal interactions ($\mathcal{B} = 5\times10^{-3}$) and let the polycrystal evolve in time. The dislocations forming the interfaces split, propel, and react while the bulk of the crystals remains unperturbed. The dislocations then proliferate across the whole sample, leading to dynamical steady states where small and lively grains are surrounded by a thick liquid phase. See also Movie S5. (*B*) Simulation of the dynamics of a single dislocation under the action of repulsive and nonreciprocal forces ($\mathcal{B} = 5\times10^{-3}$). The dislocation first glides, it then splits into a pair instead of climbing. The dislocation pair propels, interacts, splits again, leading to their proliferation and the destruction of the initial crystal order. See also Movie S6. (*C* and *D*) Schematics of glide and climb motion. (*E*) (*Left*) Force field induced by pairwise additive nonreciprocal forces having the same dipolar symmetry as in our experiments. The force field is computed in the vicinity of an isolated dislocation. (*Middle*) The arrows represent the projections of $\mathbf{F}^{\mathrm{NR}} = \gamma\dot{\mathbf{u}}^{\mathrm{NR}}$ on the Burgers vector $\mathbf{b}$. A simple shear powers the glide of the dislocation. (*Right*) The colors indicate the sign of the projection of the nonreciprocal forces on the $\mathbf{b}$ vector. The sign of the force changes across the dislocation thereby promoting a climbing dynamics. (*F*) Illustration of pairwise nonreciprocal and odd forces. Nonreciprocal forces do not feature the action–reaction symmetry, but result in a vanishing torque. Conversely, odd forces satisfy Newton's action–reaction symmetry, but their transverse direction induces a net torque on a pair of particles. (*G*) Same plots as in *E* for an odd crystal. The collection of particles interact via the same conservative repulsion and are driven out of equilibrium by transverse interactions modeled by pairwise additive forces $\mathbf{F}^{\mathrm{odd}}(\mathbf{r}) = e^{-r}\mathbf{r}^{\perp}$. (*Left*) The odd force field forms two visible vortex around an isolated dislocation. (*Middle*) The projection of the odd-force field on $\mathbf{b}$ reveals a net simple shear (i.e., a nonvanishing vorticity) acting on the dislocation; it causes its gliding dynamics. (*Right*) Unlike in the transverse direction, the off-force field hardly varies along $\mathbf{b}$. Odd forces cannot power any climb dynamics.

Discussion

Beyond Hydrodynamic Interactions: Dislocation Motion and Proliferation in Nonreciprocal Crystals. Returning to the opening question of this article, we now provide general theoretical arguments to demonstrate that our findings are not specific to driven emulsions: microscopic forces that violate Newton's third law generically promote the glide and splitting of dislocations.

To see this, we first recall the basic kinematics of dislocation dynamics; see Fig. 5 *C* and *D*. Consider a collection of particles self-organized into a periodic lattice including an isolated dislocation of Burgers vector $\mathbf{b}$. The glide of a dislocation over one lattice spacing results from minute relative displacements of the particles along the $\mathbf{b}$ direction, right above and below the dislocations. In other words, the gliding speed of a dislocation is proportional to the local shear rate across the topological defect. At a continuum level, a dislocation located at $\mathbf{r} = 0$ glides at a speed

$$v_{glide} \propto \mathbf{b}^{\perp} \cdot \boldsymbol{\nabla}(\mathbf{b} \cdot \dot{\mathbf{u}})|_{\mathbf{r}=0}, \qquad [4]$$

where $\mathbf{u}(\mathbf{r}, t)$ is the local-displacement field. Similarly, the climb speed of a dislocation is set by the local compression rate of the lattice along the axis defined by its Burgers vector, Fig. 5*D*, and $v_{climb} \propto \mathbf{b} \cdot \boldsymbol{\nabla}(\mathbf{b} \cdot \dot{\mathbf{u}})|_{\mathbf{r}=0}$.

To quantify the deformation rate of a crystal, we need to prescribe its dynamics. The displacement field of driven crystals obeys the generic momentum conservation equation:

$D_t(\rho\dot{\mathbf{u}}) = \boldsymbol{\nabla}\cdot\boldsymbol{\sigma} + \mathbf{F}(\{\mathbf{u}(\mathbf{r})\}, \mathbf{r})$, where ρ is the mass density, D_t is the convective derivative, and $\boldsymbol{\sigma}$ the stress tensor that originates from conservative interactions at the microscopic scales. When the body force acting on the crystal does not depend on the particle arrangement, $\mathbf{F}$ classically reduces to the standard sum of a dissipative drag $-\gamma\dot{\mathbf{u}}(\mathbf{r}, t)$ and of a driving force $\mathbf{F}_0(\mathbf{r})$. This situation is relevant to systems as diverse as bubble rafts mechanically sheared in a quasistatic regime (46), or Abrikosov lattices driven by an electric field and pinned by quenched disorder (47).

However, as noted first in ref. 42, the exchange of momentum between the driven particles and their surrounding environment can result in a driving force field that depends on the particles' configuration. We note it $\mathbf{F}^{NR}(\{\boldsymbol{\nabla}\mathbf{u}(\mathbf{r}, t)\})$. It is relevant when particles interact, for instance, through hydrodynamic or phoretic interactions. As such microscopic forces violate Newton's third law, they act as sources or sinks of linear momentum (27). $\mathbf{F}^{NR}$ has a simple but counterintuitive consequence: a homogeneous deformation results in a net acceleration of the crystal, but a global acceleration does not yield any deformation. Having in mind soft materials assembled from microscopic constituents, we focus on the overdamped regime where the drag force dominates inertia and simplify the equations of motion as

$$\gamma\dot{u}_i = \partial_j\sigma_{ij} + F_i^{NR}(\{\boldsymbol{\nabla}\mathbf{u}\}). \qquad [5]$$

In this limit, the local velocities are proportional to the local forces; the action of the nonreciprocal interactions can always be seen as the result of the advection of the particles by an effective flow $\dot{\mathbf{u}}^{NR} = \gamma^{-1}\mathbf{F}^{NR}$. When they arise from hydrodynamic interactions $\dot{\mathbf{u}}^{NR}$ is directly proportional to the solvent backflows caused by the motion of the particles, and $\mathbf{F}^{NR}$ can be thought as a strain-dependent drag force (42).

We are now one step away from showing that $\mathbf{F}^{NR}$ powers the dynamics of dislocations. As a matter of fact, in elastic crystals, dislocations result in nonvanishing shear, dilation, and rotation strains whose magnitude decay algebraically in space ($\nabla\mathbf{u}(\mathbf{r}) \sim 1/r$) (48). As no conservation law, or symmetry principle, requires $\nabla b_i\dot{u}_i^{NR}$ to vanish, we readily conclude from Eq. **4** that microscopic forces violating the action–reaction principle induce and sustain local displacements that promote both the glide and climb motion of dislocations: dislocations in nonreciprocal crystals are self-propelled.

To gain more intuition, in *SI Appendix*, we show how to compute $\mathbf{F}^{NR}$, and the associated dislocation speed in two cases: i) When the nonreciprocal interactions are short ranged $\mathbf{F}^{NR}$ then takes the generic form $F_i^{NR} = A_{ijk}\partial_k u_j(\mathbf{r})$, where A_{ijk} depends both on the symmetries of the forces and of the lattices; see also ref. 27. ii) When the nonreciprocal interactions are the long-range hydrodynamic forces ($\mathbf{F}_{hydro}$) relevant to our experiments, we find a simple nonlocal relation that reduces to the convolution $\mathbf{F}^{NR} \sim -\mathbf{F}_{hydro} * (\boldsymbol{\nabla}\cdot\mathbf{u})$. We further illustrate our reasoning in Fig. 5*E*. We consider an isolated dislocation in an elastic crystal whose the dynamics is ruled by Eq. **1** and show the corresponding nonreciprocal flow $\dot{\mathbf{u}}^{NR}$, along with its projection on the Burgers' vector direction, and its sign. In agreement with analytical calculations reported in *SI Appendix*, both $\mathbf{b}\cdot\boldsymbol{\nabla}(\mathbf{b}\cdot\dot{\mathbf{u}}^{NR})$ and $\mathbf{b}^{\perp}\cdot\boldsymbol{\nabla}(\mathbf{b}\cdot\dot{\mathbf{u}}^{NR})$ take finite values in the vicinity of the dislocation core, thereby promoting both its glide and climb motion.

As discussed in the previous section, we stress that the glide and climb dynamics have a very different status in elastic crystals. Unlike gliding, climbing is practically never observed due to its extensive elastic energy cost. Instead of climbing, it is energetically favorable to fission the dislocation into two defects that both glide, thereby resulting in an effective climb of the net topological charge of the dislocation pair; see Fig. 5*B* and ref. 43. This proliferation process ultimately promotes the melting of elastic crystals perturbed by strong nonreciprocal forces, regardless of their microscopic origin.

Dislocation Motion and Proliferation in Odd Crystals. We now close our discussion by commenting on the similarities and fundamental differences with another form of nonequilibrium matter: odd crystals assembled from active spinners. Prominent examples include shaken chiral grains, magnetically driven colloids, and oocyte eggs (45, 49–51). In odd crystals, the elementary units interact through forces that satisfy Newton's action–reaction symmetry. But they act in the direction transverse to the separation vectors, Fig. 5*F*: a pair of particle coupled by odd/transverse forces experience a net torque. Experiments and simulations revealed that the grain boundaries of odd polycrystals feature a lively dynamics strikingly similar to that observed in our experiments (45, 52). This dynamics can be understood within the framework we have introduced above. In short, spinners are driven by local torque sources. As soon as the particles are coupled by finite frictional interactions, this local injection of angular momentum at the microscopic level promotes the emergence of a nonvanishing vorticity $\boldsymbol{\Omega} = \frac{1}{2}\epsilon_{ij}\partial_i\dot{\mathbf{u}}_j$; see, e.g., refs. 53–55. This net vorticity is not obvious when inspecting the full flow field of Fig. 5*G*, but it becomes clear when looking at its projection in the direction defined by the Burgers vector. We can readily see that odd interactions result in a net velocity gradient across an isolated dislocation. Equation Eq. **4** then reveals that this kinematics drives the gliding motion of dislocations. Crucially, however, unlike nonreciprocal interactions, odd forces do not promote the climb dynamics of isolated dislocations. Fig. 5*G* indeed shows that the odd forces do not result in any flow gradient in the Burgers vector direction, Eq. **4**. This implies that the dislocation cannot climb. The proliferation of dislocations and the subsequent fragmentation of odd crystals is therefore fundamentally different from the nonreciprocal melting dynamics which we characterize and explain in Figs. 3 and 4. Transverse interactions cannot compete with elastic forces to fission isolated topological defects. The microscopic mechanisms leading to the fragmentation of odd crystals must involve interactions between motile dislocations which remain to be elucidated.

Conclusion and Outlook

Combining experiments and numerical simulations, we have shown that interactions that do not obey Newton's action–reaction symmetry propel and fission dislocations hosted in soft crystals. At macroscopic scales, these microscopic dynamics translate into the self-sustained remolding of grain-boundary networks and to the destruction of crystal order. Our theoretical analysis based on conservation laws and symmetry principles reveals that these phenomena are universal and should be observed in any nonequilibrium crystals challenged by nonreciprocal forces. Our work focuses on hydrodynamically driven crystals, but we provide theoretical evidence for the robustness of our findings. These insights should apply to a much broader class of nonequilibrium systems, where topological defects and nonreciprocal interactions conspire to shape the structures and dynamics of interacting units, ranging from chemically active colloids to living cells and coupled oscillators.

Data, Materials, and Software Availability. Experimental and numerical measurement data have been deposited in Zenodo (https://doi.org/10.5281/zenodo.12655234) (56).

ACKNOWLEDGMENTS. This work was partly supported by the European Research Council under the European Union's Horizon 2020 research and innovation program (Grant Agreement No. [101019141]) (D.B.). We thank Ephraim Bililign, Yehuda Ganan, Michel Fruchart, and Colin Scheibner for illuminating discussions.

Author affiliations: [a]Univ. Lyon, ENS de Lyon, Univ. Claude Bernard, CNRS, Laboratoire de Physique, Lyon F-69342, France; [b]Pôle d'Etudes et Recherche de Lacq, Total SA, Lacq BP 47-64170, France; [c]James Franck Institute, University of Chicago, Chicago, IL 60637; and [d]Department of Physics, University of Chicago, Chicago, IL 60637

1. J. Happel, H. Brenner, *Low Reynolds Number Hydrodynamics: With Special Applications to Particulate Media (Springer Science &* Business Media, 2012), vol. 1.
2. R. Chajwa, N. Menon, S. Ramaswamy, Kepler orbits in pairs of disks settling in a viscous fluid. *Phys. Rev. Lett.* **122**, 224501. (2019).
3. J. F. Brady, G. Bossis, Stokesian dynamics. *Annu. Rev. Fluid Mech.* **20**, 111–157 (1988).
4. J. Palacci, S. Sacanna, A. P. Steinberg, D. J. Pine, P. M. Chaikin, *Living crystals of light-activated colloidal surfers* (Science New York, N.Y.), 2013), vol. 339, pp. 936–940.
5. R. Soto, R. Golestanian, Self-assembly of catalytically active colloidal molecules: Tailoring activity through surface chemistry. *Phys. Rev. Lett.* **112**, 068301. (2014).
6. M. Fruchart, R. Hanai, P. B. Littlewood, V. Vitelli, Non-reciprocal phase transitions. *Nature* **592**, 363–369 (2021).
7. J. Veenstra *et al*., Non-reciprocal topological solitons in active metamaterials. *Nature* **627**, 528–533 (2024).
8. J. R. Seymour, D. R. Brumley, R. Stocker, J. B. Raina, Swimming towards each other: The role of chemotaxis in bacterial interactions. *Trends Microbiol.* **32**, 640–649 (2024).
9. A. Cavagna, I. Giardina, Bird flocks as condensed matter. *Annu. Rev. Condens. Matter Phys.* **5**, 183–207 (2014).
10. I. Karamouzas, B. Skinner, S. J. Guy, Universal power law governing pedestrian interactions. *Phys. Rev. Lett.* **113**, 238701. (2014).
11. É. Guazzelli, J. Hinch, Fluctuations and instability in sedimentation. *Annu. Rev. Fluid Mech.* **43**, 97–116 (2011).
12. S. Ramaswamy, Issues in the statistical mechanics of steady sedimentation. *Adv. Phys.* **50**, 297–341 (2001).
13. T. Beatus, I. Shani, R. H. Bar-Ziv, T. Tlusty, Two-dimensional flow of driven particles: A microfluidic pathway to the non-equilibrium frontier. *Chem. Soc. Rev.* **46**, 5620–5646 (2017).
14. J. M. Crowley, Viscosity-induced instability of a one-dimensional lattice of falling spheres. *J. Fluid Mech.* **45**, 151–159 (1971).
15. T. Beatus, T. Tlusty, R. Bar-Ziv, Phonons in a one-dimensional microfluidic crystal. *Nat. Phys.* **2**, 743–748 (2006).
16. N. Desreumaux, N. Florent, E. Lauga, D. Bartolo, Active and driven hydrodynamic crystals. *Eur. Phys. J. E* **35**, 68 (2012).
17. R. Chajwa, N. Menon, S. Ramaswamy, R. Govindarajan, Waves, algebraic growth, and clumping in sedimenting disk arrays. *Phys. Rev. X* **10**, 041016. (2020).
18. I. Saeed, H. K. Pak, T. Tlusty, Quasiparticles, flat bands and the melting of hydrodynamic matter. *Nat. Phys.* **19**, 536–544 (2023).
19. R. Soto, R. Golestanian, Self-assembly of catalytically active colloidal molecules: Tailoring activity through surface chemistry. *Phys. Rev. Lett.* **112**, 068301. (2014).
20. A. V. Ivlev *et al*., Statistical mechanics where Newton's third law is broken. *Phys. Rev. X* **5**, 011035. (2015).
21. C. H. Meredith *et al*., Predator-prey interactions between droplets driven by non-reciprocal oil exchange. *Nat. Chem.* **12**, 1136–1142 (2020).
22. Z. You, A. Baskaran, M. C. Marchetti, Nonreciprocity as a generic route to traveling states. *Proc. Natl. Acad. Sci. U.S.A.* **117**, 19767–19772 (2020).
23. S. Saha, J. Agudo-Canalejo, R. Golestanian, Scalar active mixtures: The nonreciprocal Cahn-Hilliard model. *Phys. Rev. X* **10**, 041009. (2020).
24. M. Fruchart, R. Hanai, P. B. Littlewood, V. Vitelli, Non-reciprocal phase transitions. *Nature* **592**, 363–369 (2021).
25. S. Osat, R. Golestanian, Non-reciprocal multifarious self-organization. *Nat. Nanotechnol.* **18**, 79–85 (2023).
26. R. Golestanian, in *"Phoretic active matter" in Active Matter and Nonequilibrium Statistical Physics: Lecture Notes of the Les Houches Summer School*, September 2018, J. Tailleur, G Gompper, M. C. Marchetti, J. M. Yeomans, C. Salomon, Eds. (Oxford University Press, 2022). vol. 112.
27. A. Poncet, D. Bartolo, When soft crystals defy Newton's third law: Nonreciprocal mechanics and dislocation motility. *Phys. Rev. Lett.* **128**, 048002. (2022).
28. S. Maity, A. Morin, Spontaneous demixing of binary colloidal flocks. *Phys. Rev. Lett.* **131**, 178304. (2023).
29. A. Dinelli *et al*., Non-reciprocity across scales in active mixtures. *Nat. Commun.* **14**, 7035 (2023).
30. J. Chen *et al*., Emergent chirality and hyperuniformity in an active mixture with nonreciprocal interactions. *Phys. Rev. Lett.* **132**, 118301. (2024).
31. Y. Rouzaire, D. Levis, I. Pagonabarraga, Non-reciprocal interactions reshape topological defect annihilation. https://arxiv.org/abs/2401.12637 (Accessed 17 March 2025).
32. B. I. Halperin, D. R. Nelson, Theory of two-dimensional melting. *Phys. Rev. Lett.* **41**, 121–124 (1978).
33. D. R. Nelson, B. I. Halperin, Dislocation-mediated melting in two dimensions. *Phys. Rev. B* **19**, 2457–2484 (1979).
34. A. P. Young, Melting and the vector coulomb gas in two dimensions. *Phys. Rev. B* **19**, 1855–1866 (1979).
35. K. Zahn, R. Lenke, G. Maret, Two-stage melting of paramagnetic colloidal crystals in two dimensions. *Phys. Rev. Lett.* **82**, 2721–2724 (1999).
36. H. H. von Grünberg, P. Keim, K. Zahn, G. Maret, Elastic behavior of a two-dimensional crystal near melting. *Phys. Rev. Lett.* **93**, 255703. (2004).
37. U. Gasser, C. Eisenmann, G. Maret, P. Keim, Melting of crystals in two dimensions. *ChemPhysChem* **11**, 963–970 (2010).
38. S. Deutschländer, P. Dillmann, G. Maret, P. Keim, Kibble-Zurek mechanism in colloidal monolayers. *Proc. Natl. Acad. Sci. U.S.A.* **112**, 6925–6930 (2015).
39. N. Desreumaux, J. B. Caussin, R. Jeanneret, E. Lauga, D. Bartolo, Hydrodynamic fluctuations in confined particle-laden fluids. *Phys. Rev. Lett.* **111**, 118301. (2013).
40. M. Kardar, *Statistical Physics of Fields* (Cambridge University Press, 2007).
41. P. Oswald, *Rheophysics* (Cambridge University Press, 2009).
42. R. Lahiri, S. Ramaswamy, Are steadily moving crystals unstable? *Phys. Rev. Lett.* **79**, 1150–1153 (1997).
43. W. T. M. Irvine, A. D. Hollingsworth, D. G. Grier, P. M. Chaikin, Dislocation reactions, grain boundaries, and irreversibility in two-dimensional lattices using topological tweezers. *Proc. Natl. Acad. Sci. U.S.A.* **110**, 15544–15548 (2013).
44. G. Briand, O. Dauchot, Crystallization of self-propelled hard discs. *Phys. Rev. Lett.* **117**, 098004. (2016).
45. E. S. Bililign *et al*., Motile dislocations knead odd crystals into whorls. *Nat. Phys.* **18**, 212–218 (2022).
46. W. L. Bragg, J. F. Nye, A dynamical model of a crystal structure. *Proc. R. Soc. Lond. Ser. A, Math. Phys. Sci.* **190**, 474–481 (1947).
47. G. Blatter, M. V. Feigel'man, V. B. Geshkenbein, A. I. Larkin, V. M. Vinokur, Vortices in high-temperature superconductors. *Rev. Mod. Phys.* **66**, 1125–1388 (1994).
48. L. D. Landau, E. M. Lifshitz, *Theory of Elasticity* (Pergamon Press, Oxford, UK/New York, NY, 1986).
49. C. Scheibner *et al*., Odd elasticity. *Nat. Phys.* **16**, 475–480 (2020).
50. T. H. Tan *et al*., Odd dynamics of living chiral crystals. *Nature* **607**, 287–293 (2022).
51. M. Fruchart, C. Scheibner, V. Vitelli, Odd viscosity and odd elasticity. *Annu. Rev. Condens. Matter Phys.* **14**, 471–510 (2023).
52. C. B. Caporusso, G. Gonnella, D. Levis, Phase coexistence and edge currents in the chiral Lennard-Jones fluid. *Phys. Rev. Lett.* **132**, 168201. (2024).
53. J. C. Tsai, F. Ye, J. Rodriguez, J. P. Gollub, T. C. Lubensky, A chiral granular gas. *Phys. Rev. Lett.* **94**, 214301. (2005).
54. D. J. Bonthuis, D. Horinek, L. Bocquet, R. R. Netz, Electrohydraulic power conversion in planar nanochannels. *Phys. Rev. Lett.* **103**, 144503. (2009).
55. V. Soni *et al*., The odd free surface flows of a colloidal chiral fluid. *Nat. Phys.* **15**, 1188–1194 (2019).
56. S. Guillet *et al*., Supporting datas for "Melting of non reciprocal solids: how dislocation propel and fission in flowing crystals." Zenodo. https://doi.org/10.5281/zenodo.12655234. Deposited 25 March 2025.